



Cite this: *RSC Adv.*, 2019, 9, 18042

Infrared and Raman spectra of $\text{Bi}_2\text{O}_2\text{X}$ and Bi_2OX_2 ($\text{X} = \text{S}, \text{Se}, \text{and Te}$) studied from first principles calculations†

Yao-Di Xu,^a Cong Wang,^a Yang-Yang Lv,^a Y. B. Chen,^b Shu-Hua Yao^{acd} and Jian Zhou^{bd*}

The bismuth oxychalcogenide compounds contain many different kinds of materials, such as $\text{Bi}_2\text{O}_2\text{X}$ and Bi_2OX_2 ($\text{X} = \text{S}, \text{Se}, \text{and Te}$). These materials have different but similar layered crystal structures and exhibit various interesting physical properties. Here, we have theoretically investigated their Raman and infrared spectra by first principles calculations based on density functional theory. It is found that in $\text{Bi}_2\text{O}_2\text{Se}$ the calculated frequency of the A_{1g} Raman active mode is in good agreement with the experimental measurements while the other three modes are ambiguous or not observed yet. The Raman and infrared spectra of other materials are also presented and need further confirmation. Our work provides the structural fingerprints of these materials, which could be helpful in identifying the crystal structures in future experiments.

Received 6th April 2019
Accepted 12th May 2019

DOI: 10.1039/c9ra02584g

rsc.li/rsc-advances

1 Introduction

In recent years, bismuth oxychalcogenide materials Bi-O-X ($\text{X} = \text{S}, \text{Se}, \text{and Te}$) have attracted more and more attention. Among these materials, $\text{Bi}_2\text{O}_2\text{Se}$, synthesized more than forty years ago,¹ is one of the most studied materials and has now become a very hot topic due to its various and interesting physical properties. First, $\text{Bi}_2\text{O}_2\text{Se}$ was suggested to be a good thermoelectric material.²⁻⁷ In 2010, Ruleova *et al.* reported the thermoelectric properties of $\text{Bi}_2\text{O}_2\text{Se}$ and they found that $\text{Bi}_2\text{O}_2\text{Se}$ is an n-type semiconductor with a very low thermal conductivity and a relatively high figure of merit ZT about 0.2 at 800 K.² Several theoretical works were also conducted to explore its thermoelectric properties.⁸⁻¹¹ Second, $\text{Bi}_2\text{O}_2\text{Se}$ has an ultrahigh electron mobility.¹²⁻¹⁷ An earlier work in 2012 found that the room temperature Hall mobility of $\text{Bi}_2\text{O}_2\text{Se}$ single crystal was on the order of $300 \text{ cm}^2 \text{ s}^{-1} \text{ V}^{-1}$.¹² Recently, it was found that the low temperature (about 2 K) Hall mobility can reach more than $2.0 \times 10^4 \text{ cm}^2 \text{ s}^{-1} \text{ V}^{-1}$ in $\text{Bi}_2\text{O}_2\text{Se}$ thin film¹³⁻¹⁵ and $4.0 \times 10^4 \text{ cm}^2 \text{ s}^{-1} \text{ V}^{-1}$ in $\text{Bi}_2\text{O}_2\text{Se}$ single crystal.¹⁶ Very recently, we have

observed a superior Hall mobility of $2.2 \times 10^5 \text{ cm}^2 \text{ s}^{-1} \text{ V}^{-1}$ at 2 K in a high quality $\text{Bi}_2\text{O}_2\text{Se}$ single crystal.¹⁷ The high mobility in $\text{Bi}_2\text{O}_2\text{Se}$ is possibly due to the self-modulation doping, *i.e.* the electron donor states lie above the lowest conduction band, not in the middle of the band gap.¹⁸ Furthermore, high mobility usually induces a large magnetoresistance (MR),¹⁹ which was also observed in $\text{Bi}_2\text{O}_2\text{Se}$. A longitudinal MR of about 600% (at 15 Tesla and 2 K) and 9000% (at 9 Tesla and 2 K) in $\text{Bi}_2\text{O}_2\text{Se}$ single crystals was observed in two recent experiments.^{16,17} Third, due to its high mobility and suitable band gap (about 0.8 eV), $\text{Bi}_2\text{O}_2\text{Se}$ was used in optoelectronic devices and infrared (IR) photo-detectors.²⁰⁻²²

$\text{Bi}_2\text{O}_2\text{Te}$ has the same crystal structure as that of $\text{Bi}_2\text{O}_2\text{Se}$, but it is much less studied. Luu and Vaqueiro found that $\text{Bi}_2\text{O}_2\text{Te}$ ceramics is an n-type semiconductor with a smaller band gap (0.23 eV), electron mobility ($47 \text{ cm}^2 \text{ s}^{-1} \text{ V}^{-1}$ at room temperatures), and ZT (0.13 at 573 K), compared with those of $\text{Bi}_2\text{O}_2\text{Se}$.²³ The similar compound $\text{Bi}_2\text{O}_2\text{S}$ is also less studied. $\text{Bi}_2\text{O}_2\text{S}$ was first synthesized in 1984 and it has a different crystal structure to that of $\text{Bi}_2\text{O}_2\text{Se}$.²⁴ There are only a few studies on its optical properties.²⁵⁻²⁷ For example, it was found that $\text{Bi}_2\text{O}_2\text{S}$ has an indirect band gap of 1.12 eV and it is an excellent photoelectric material.²⁷

On the other hand, there is another kind of bismuth oxychalcogenides Bi_2OX_2 ($\text{X} = \text{S}, \text{Se}, \text{and Te}$), which all share the same tetragonal lattice system. Among them, Bi_2OS_2 has been experimentally synthesized recently and it was a candidate as an optoelectronic material in the near-IR region.²⁸ First principles calculations indicated that the two-dimensional Bi_2OS_2 nano-sheet possesses a direct band gap and an ultrahigh electron mobility (up to $2.6 \times 10^4 \text{ cm}^2 \text{ s}^{-1} \text{ V}^{-1}$).²⁹ To the best of our knowledge, Bi_2OSe_2 and Bi_2OTe_2 have not been synthesized

^aNational Laboratory of Solid State Microstructures and Department of Materials Science and Engineering, Nanjing University, Nanjing 210093, China. E-mail: zhoujian@nju.edu.cn

^bNational Laboratory of Solid State Microstructures and Department of Physics, Nanjing University, Nanjing 210093, China

^cCollaborative Innovation Center of Advanced Microstructures, Nanjing University, Nanjing, 210093, China

^dJiangsu Key Laboratory of Artificial Functional Materials, Nanjing University, Nanjing 210093, China

† Electronic supplementary information (ESI) available. See DOI: 10.1039/c9ra02584g



experimentally. However, first principles calculations showed that they have the same crystal structure as that of $\text{Bi}_2\text{O}_2\text{S}_2$.³⁰ In particular, the calculated electron and hole effective mass of Bi_2OX_2 is very small. For example, the effective mass of Bi_2OTe_2 is only 0.02 and 0.012 for electron and hole.³⁰ Another theoretical study indicated that Bi_2OX_2 materials show promising characteristics in applications for solar cells and thermoelectric devices.³¹

Besides $\text{Bi}_2\text{O}_2\text{X}$ and Bi_2OX_2 , the first BiS_2 family superconductor $\text{Bi}_4\text{O}_4\text{S}_3$ was studied over the past few years.^{32,33} Later, it was found that $\text{Bi}_4\text{O}_4\text{S}_3$ is a mixture of the two phases, Bi_2OS_2 and $\text{Bi}_3\text{O}_2\text{S}_3$.³⁴ The former is non-superconducting, while the latter is superconducting.^{34–36}

Therefore, we can see that the Bi–O–X system contains many kinds of materials with various interesting physical properties. From the experimental point of view, it is of course very important to identify the structure of the grown crystal from the many similar Bi–O–X materials. In this regard, Raman and IR spectra are convenient and powerful methods to provide the structural fingerprints of materials. However, we find that the Raman and IR studies of these materials are quite lacking. Only a few works about the Raman spectra of $\text{Bi}_2\text{O}_2\text{Se}$ and $\text{Bi}_2\text{O}_2\text{Te}$ have been reported until now.^{14,16,37,38} For this reason, we have systematically calculated the phonon, irreducible representations, Raman and IR spectra, vibrational eigenvectors of optical phonons, and polarized Raman configurations of six materials: $\text{Bi}_2\text{O}_2\text{X}$ and Bi_2OX_2 . We mainly present the results of $\text{Bi}_2\text{O}_2\text{Se}$ and $\text{Bi}_2\text{O}_2\text{Te}$ since they can be compared with other works. The Raman and IR spectra of the other four materials are also given briefly and could be referenced by future experiments.

2 Computational details

The vibrational properties of $\text{Bi}_2\text{O}_2\text{X}$ and Bi_2OX_2 ($\text{X} = \text{S}, \text{Se}, \text{and Te}$) are calculated by density functional theory (DFT) implemented in the Vienna *ab initio* simulation package (VASP).^{39,40} The projected augmented wave method^{41,42} and the generalized gradient approximation with the Perdew–Burke–Ernzerhof exchange–correlation functional⁴³ are used. The DFT-D3 method^{44,45} is used to correct the van der Waals interactions in these layered materials. The plane-wave cutoff energy is 520 eV for all materials. Both the internal atomic positions and the lattice constants are allowed to relax until the maximal residual Hellmann–Feynman forces on atoms are smaller than $0.002 \text{ eV } \text{\AA}^{-1}$. The k -mesh is $8 \times 8 \times 2$ for $\text{Bi}_2\text{O}_2\text{S}$ and Bi_2OX_2 and $8 \times 8 \times 8$ for $\text{Bi}_2\text{O}_2\text{Se}$ and $\text{Bi}_2\text{O}_2\text{Te}$. The Phonopy package⁴⁶ is used to calculate the phonon frequencies, eigenvectors and irreducible representations of the materials. The crystal structures and eigenvectors are plotted by the VESTA program.⁴⁷

The IR and Raman activity of phonon modes can be analyzed by their irreducible representations. However their intensities need additional calculations. The IR intensity of a phonon mode is given by the corresponding oscillator strength:⁴⁸

$$f(\nu) = \sum_{\alpha} \left| \sum_{s\beta} Z_{\alpha\beta}^*(s) e_{\beta}(s, \nu) \right|^2$$

where the $e_{\beta}(s, \nu)$ is the normalized vibrational eigenvector of the ν th phonon mode of the s th atom in the unit cell. α and β are the Cartesian coordinates: x, y, z . $Z_{\alpha\beta}^*(s)$ is the Born effective charge tensor of the s th atom. The Born effective charge tensor and the phonon eigenvectors are calculated by the density functional perturbation theory (DFPT) implemented in the VASP code. This method has been applied to different material systems.^{48–51}

The off-resonance Raman intensity of a phonon mode can be estimated by calculating the derivative of the macroscopic dielectric tensor with respect to the normal mode coordinate:⁵²

$$I_{\text{Raman}}(\nu) \propto \frac{\partial \epsilon^{\infty}}{\partial Q(\nu)}$$

where the ϵ^{∞} is the macroscopic high-frequency dielectric constant and $Q(\nu)$ is the normal mode coordinate of the ν th phonon mode. In practice, the derivative is replaced by the central difference based on the macroscopic dielectric matrix evaluated at positive and negative displacement along the phonon mode $Q(\nu)$. The macroscopic dielectric matrix is also calculated by the DFPT method in the VASP code. This method has also been applied to different material systems.^{53,54}

3 Results and discussions

3.1 Crystal structures of $\text{Bi}_2\text{O}_2\text{X}$ and Bi_2OX_2

The six materials $\text{Bi}_2\text{O}_2\text{X}$ and Bi_2OX_2 ($\text{X} = \text{S}, \text{Se}, \text{and Te}$) have three different crystal structures. $\text{Bi}_2\text{O}_2\text{S}$ belongs to a primitive orthorhombic lattice with a space group $Pnmm$ (no. 58),²⁴ while $\text{Bi}_2\text{O}_2\text{Se}$ and $\text{Bi}_2\text{O}_2\text{Te}$ possess a body centered tetragonal lattice with a space group $I4/mmm$ (no. 139).^{1,13,23} On the other hand, Bi_2OX_2 have a primitive tetragonal lattice with a space group $P4/nmm$ (no. 129).^{28,55} All the materials show layered structures as shown in Fig. 1. $\text{Bi}_2\text{O}_2\text{X}$ consists of two Bi_2O_2 and two X layers, while Bi_2OX_2 is composed of one Bi_2O_2 and two BiX_2 layers in a unit cell. Although the symmetries of $\text{Bi}_2\text{O}_2\text{S}$ and $\text{Bi}_2\text{O}_2\text{Se}$ are totally different, the structure of $\text{Bi}_2\text{O}_2\text{S}$ is a slightly distorted form of $\text{Bi}_2\text{O}_2\text{Se}$.²⁴ Therefore, the difference between the two structures shown in Fig. 1(a) and (b) is hardly visible to the naked eye. All the structures shown in Fig. 1 contain ten atoms in the unit cell. However, $\text{Bi}_2\text{O}_2\text{Se}$ and $\text{Bi}_2\text{O}_2\text{Te}$ shown in

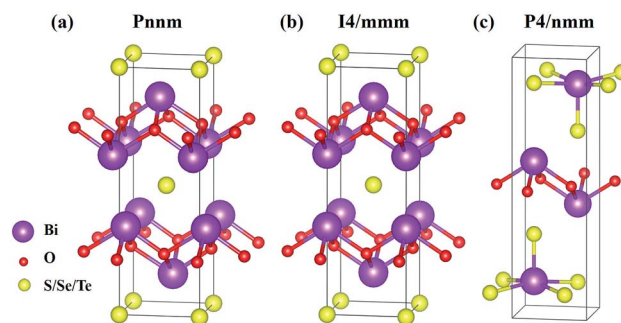


Fig. 1 Layered crystal structures of (a) orthorhombic $\text{Bi}_2\text{O}_2\text{S}$, (b) tetragonal $\text{Bi}_2\text{O}_2\text{Se}$ and $\text{Bi}_2\text{O}_2\text{Te}$, (c) tetragonal Bi_2OS_2 , Bi_2OSe_2 , and Bi_2OTe_2 . The purple, red, and yellow balls represent Bi, O, and S/Se/Te atoms respectively.



Table 1 Calculated lattice constants of $\text{Bi}_2\text{O}_2\text{X}$ and Bi_2OX_2 ($\text{X} = \text{S}, \text{Se},$ and Te) in the unit of Å. Other theoretical and experimental results are also given for comparison

Symmetry	Material	Reference	<i>a</i>	<i>b</i>	<i>c</i>
Orthorhombic <i>Pnmm</i>	$\text{Bi}_2\text{O}_2\text{S}$	This work	3.837	3.848	11.94
		Experiment ²⁴	3.840	3.874	11.92
		Theory ³⁰	3.87	3.89	11.99
Tetragonal <i>I4/mmm</i>	$\text{Bi}_2\text{O}_2\text{Se}$	This work	3.891	3.891	12.20
		Experiment ¹	3.891	3.891	12.21
		Experiment ¹³	3.88	3.88	12.16
	$\text{Bi}_2\text{O}_2\text{Te}$	Theory ³⁰	3.91	3.91	12.38
		This work	3.984	3.984	12.65
		Experiment ²³	3.980	3.980	12.70
Tetragonal <i>P4/nmm</i>	Bi_2OS_2	Theory ³⁰	4.01	4.01	12.63
		This work	3.950	3.950	13.84
		Experiment ²⁸	3.961	3.961	13.80
	Bi_2OSe_2	Experiment ⁵⁵	3.964	3.964	13.83
		Theory ³⁰	3.96	3.96	13.69
		This work	4.044	4.044	14.56
	Bi_2OTe_2	Theory ³⁰	4.05	4.05	14.46
		This work	4.193	4.193	15.81
		Theory ³⁰	4.17	4.17	15.99

Fig. 1(b) is a conventional cell, which in fact contains two primitive cells.

It is noted that among the six materials, to the best of our knowledge, Bi_2OSe_2 and Bi_2OTe_2 have not been synthesized experimentally. Their crystal structures are predicted to be the same as that of Bi_2OS_2 by first principles calculations.³⁰

The calculated lattice constants in this work with the DFT-D3 correction are listed in Table 1. It is obvious that our calculated results are well consistent with the experimental measurements with the largest difference less than 1%. Our results are also in good agreement with other theoretical work.³⁰

With the optimized structures, the zone-centered phonon modes, irreducible representations, IR and Raman spectra of the six materials are calculated. In the following subsections, we first present the detailed results of $\text{Bi}_2\text{O}_2\text{Se}$ and $\text{Bi}_2\text{O}_2\text{Te}$ since both materials have the same crystal structure and the Raman spectrum of $\text{Bi}_2\text{O}_2\text{Se}$ is better studied than other materials. Then the brief results of $\text{Bi}_2\text{O}_2\text{S}$ and Bi_2OX_2 are also given.

3.2 *I4/mmm* tetragonal $\text{Bi}_2\text{O}_2\text{Se}$ and $\text{Bi}_2\text{O}_2\text{Te}$

The calculated zone-centered optical phonon frequencies of $\text{Bi}_2\text{O}_2\text{Se}$ and $\text{Bi}_2\text{O}_2\text{Te}$ are listed in Table 2. The highest phonon frequency of $\text{Bi}_2\text{O}_2\text{Se}$ is about 433.3 cm^{-1} , while it is only 396.1 cm^{-1} in $\text{Bi}_2\text{O}_2\text{Te}$ due to the heavier atom mass. $\text{Bi}_2\text{O}_2\text{Se}$ and $\text{Bi}_2\text{O}_2\text{Te}$ have the same space group of *I4/mmm* (point group D_{4h}), and their irreducible representations at the Γ point in the Brillouin zone are:

$$\Gamma_{\text{acoustic}} = E_u + A_{2u}$$

$$\Gamma_{\text{optic}} = 2E_u + 2A_{2u} + 2E_g + A_{1g} + B_{1g}$$

There are five atoms in the primitive cell of $\text{Bi}_2\text{O}_2\text{Se}$, therefore we can find three acoustic and twelve optical modes. These irreducible representations are also assigned to each optical phonon mode as shown in Table 2. According to the character table of the D_{4h} point group, the E_u and A_{2u} modes are IR active, while the E_g , A_{1g} , and B_{1g} modes are Raman active in $\text{Bi}_2\text{O}_2\text{Se}$ and $\text{Bi}_2\text{O}_2\text{Te}$. Therefore, both materials have four Raman active (two double degenerated E_g mode and two non-degenerated A_{1g} and B_{1g} modes) and four IR active modes (two double degenerated E_u modes and two non-degenerated A_{2u} modes), as indicated in Table 2.

Recently, there have been two joint experimental and theoretical works by Pereira *et al.*³⁷ and Cheng *et al.*,³⁸ in which the phonon frequencies of $\text{Bi}_2\text{O}_2\text{Se}$ and $\text{Bi}_2\text{O}_2\text{Te}$ are also calculated. We listed their data in Table 2 for comparison. It is found that most of the calculated frequencies are in good agreement with ours, except for the two high-frequency IR active modes (E_u and A_{2u}) in $\text{Bi}_2\text{O}_2\text{Se}$, which have a maximal discrepancy of about 25 cm^{-1} . Phonon frequencies depend on the second derivative of the total energy, therefore the accuracy of the phonon calculation is usually not as good as the ones of the total energy calculations. Many parameters, such as the exchange–correlation functional, will affect the theoretical phonon frequencies. Therefore, we think such differences between these works are acceptable in phonon calculations.

We also illustrate the vibrational eigenvectors of $\text{Bi}_2\text{O}_2\text{Se}$ in Fig. 2. It is found that the two low-frequency Raman active modes (E_g and A_{1g}) are related to the in-plane and out-of-plane

Table 2 Calculated frequencies and Mulliken symbols of zone-centered optical phonon modes of $\text{Bi}_2\text{O}_2\text{Se}$ and $\text{Bi}_2\text{O}_2\text{Te}$. The theoretical frequencies in other works by Pereira³⁷ and Cheng³⁸ are also listed for comparison. Raman or IR activity of each mode is also indicated by "Raman" and "IR". The unit of the phonon frequency is cm^{-1}

Symmetry	$\text{Bi}_2\text{O}_2\text{Se}$			$\text{Bi}_2\text{O}_2\text{Te}$		Activity
	This work	Pereira ³⁷	Cheng ³⁸	This work	Cheng ³⁸	
E_u	54.8	59.2		56.4		IR
A_{2u}	65.0	64.5		63.3		IR
E_g	67.3	72.0	67.99	69.1	67.01	Raman
A_{1g}	162.9	165.7	159.89	150.4	147.48	Raman
E_u	268.0	293.9		243.6		IR
B_{1g}	354.3	369.4	364.02	336.0	340.33	Raman
A_{2u}	377.8	402.8		347.3		IR
E_g	433.3	444.0	428.68	396.1	386.15	Raman



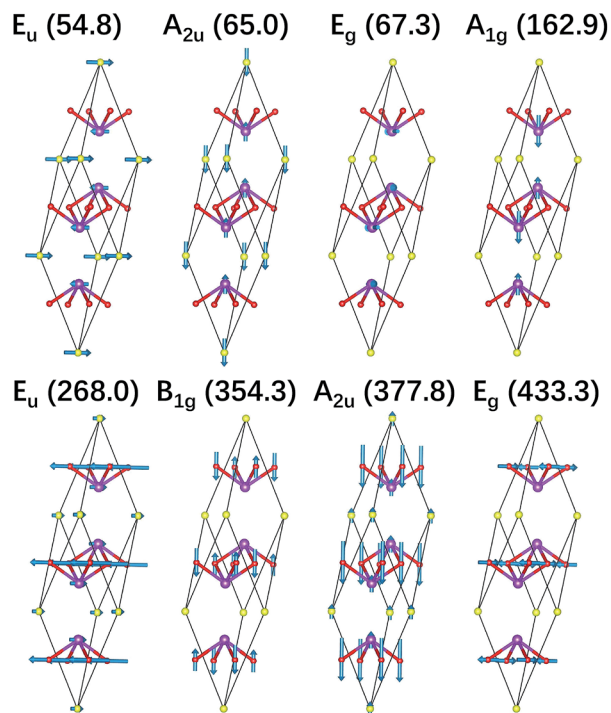


Fig. 2 Vibrational eigenvectors of the zone-centered optical phonon modes shown in the primitive cell of $\text{Bi}_2\text{O}_2\text{Se}$. The purple, red, and yellow balls represent Bi, O, and Se atoms respectively.

vibrations of Bi atoms, respectively. While the two high-frequency Raman active modes (B_{1g} and E_g) represent the out-of-plane and in-plane vibrations of O atoms, respectively. Vibrations of Se atoms are not involved in any Raman active modes. The two low-frequency IR active modes (E_u and A_{2u}) are related to the in-plane and out-of-plane vibrations of Bi and Se atoms, respectively. While the two high-frequency IR active modes (E_u and A_{2u}) mainly represent the in-plane and out-of-plane vibrations of O atoms, respectively. The vibrational eigenvectors of $\text{Bi}_2\text{O}_2\text{Te}$ are similar to those of $\text{Bi}_2\text{O}_2\text{Se}$, which are not shown here.

Then we present a detailed analysis about the polarized configurations for the Raman active modes of $\text{Bi}_2\text{O}_2\text{Se}$ and $\text{Bi}_2\text{O}_2\text{Te}$. The Raman tensors of the D_{4h} point group can be written as:

$$P(E_g) = \begin{pmatrix} 0 & 0 & 0 \\ 0 & 0 & e \\ 0 & e & 0 \end{pmatrix}, \begin{pmatrix} 0 & 0 & -e \\ 0 & 0 & 0 \\ -e & 0 & 0 \end{pmatrix}$$

$$P(A_{1g}) = \begin{pmatrix} a & 0 & 0 \\ 0 & a & 0 \\ 0 & 0 & b \end{pmatrix} \quad P(B_{1g}) = \begin{pmatrix} c & 0 & 0 \\ 0 & -c & 0 \\ 0 & 0 & 0 \end{pmatrix}$$

Qualitatively, the Raman intensity I of a phonon mode can be calculated by the formula $I \propto |e_i \cdot P \cdot e_s|^2$, where e_i and e_s are polarization directions of the incident and scattered light and P is the Raman tensor given above. In Table 3, we present the non-equivalent polarized configurations for the Raman active modes

Table 3 The right angle and back scattering geometries in the polarized configurations of Raman active modes of $\text{Bi}_2\text{O}_2\text{Se}$ and $\text{Bi}_2\text{O}_2\text{Te}$. The modes that can be observed in the configuration are indicated by the mark ✓

Configurations	A_{1g}	B_{1g}	E_g
$X(YY)Z$	✓	✓	
$Z(XX)Y$	✓	✓	
$X(ZZ)Y$	✓		
$X(YZ)Y$			✓
$Z(XZ)X$			✓
$-Z(XX)Z$	✓	✓	
$-Y(XX)Y$	✓	✓	
$-X(ZZ)X$	✓		
$-X(YZ)X$			✓

of $\text{Bi}_2\text{O}_2\text{Se}$ and $\text{Bi}_2\text{O}_2\text{Te}$. In the configuration notation $A(BC)D$, A and D represent the propagation directions of the incident and scattered light respectively, while B and C represent the polarization directions of the incident and scattered light respectively. In the right angle scattering geometry, the propagation directions of the incident and scattered light are orthogonal (first five configurations in Table 3). In the back scattering geometry, the propagation directions of the incident and scattered light are anti-parallel (last four configurations in Table 3).

From Table 3, it is interesting to find that the E_g mode cannot be observed with the A_{1g} and B_{1g} ones simultaneously under the same polarized configuration. Also, only one A_{1g} mode can be observed in the polarized configurations: $X(ZZ)Y$ or $-X(ZZ)X$. Therefore, all of the Raman active modes can be well identified under different polarized configurations. Of course, in this case, the frequencies of the four Raman active modes in $\text{Bi}_2\text{O}_2\text{Se}$ and $\text{Bi}_2\text{O}_2\text{Te}$ are well separated and therefore it is quite easy to identify these modes in experiments according to their frequencies without considering their polarized configurations.

IR and Raman intensities of $\text{Bi}_2\text{O}_2\text{Se}$ and $\text{Bi}_2\text{O}_2\text{Te}$ are also calculated directly by first principles calculations based on the

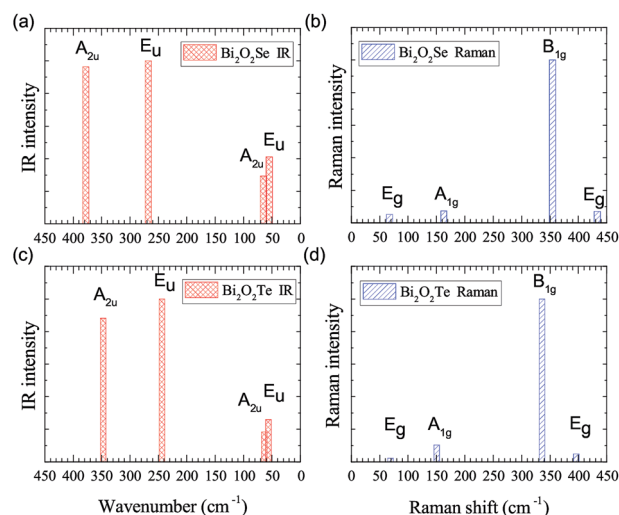


Fig. 3 Calculated IR and Raman intensities (arbitrary unit) of $\text{Bi}_2\text{O}_2\text{Se}$ and $\text{Bi}_2\text{O}_2\text{Te}$.



Table 4 Comparison between calculated and experimental Raman frequencies of Bi₂O₂Se

	Raman frequency (cm ⁻¹)
This work	67.3 (E _g), 162.9 (A _{1g}), 354.3 (B _{1g}), 433.3 (E _g)
Experiment ¹⁴	100, 159
Experiment ¹⁶	84/90 (E _g ²), 159 (A _{1g})
Experiment ³⁷	159.2 (A _{1g})
Experiment ³⁸	160 (A _{1g})

equations in Section II, which are shown in Fig. 3. From Fig. 3(a) and (c), we can see that the two high-frequency IR active modes (E_u and A_{2u}) have relatively higher intensities than those of the low-frequency modes (E_u and A_{2u}). On the other hand, in Fig. 3(b) and (d), the Raman active mode B_{1g} has the highest intensity for both materials, while the other three modes have much lower intensities.

Recently, there have been four experimental works,^{14,16,37,38} in which the Raman spectrum of Bi₂O₂Se was given. Wu *et al.* have synthesized the atomically thin two-dimensional and the bulk Bi₂O₂Se crystals and they observed two Raman peaks located at about 100 and 159 cm⁻¹.¹⁴ Tong *et al.* have grown high-quality Bi₂O₂Se single crystals and found two main Raman peaks located at around 90 and 159 cm⁻¹, which are associated with the symmetries of E_g² and A_{1g}² respectively.¹⁶ However, it seems that the E_g² mode in their figure is made up of two adjacent peaks located at 84 and 90 cm⁻¹.¹⁶ Pereira *et al.* studied the physical properties of Bi₂O₂Se at high pressure, in which they only observed one most intense Raman peak at around 159.2 cm⁻¹ at room pressure.³⁷ The theoretical low-frequency E_g mode (near 70 cm⁻¹) can only be observed at high pressure.³⁷ Cheng *et al.* have measured the Raman spectra of Bi₂O₂Se and Bi₂O₂Te.³⁸ These results are summarized in Table 4, from which we can see that the Raman active mode A_{1g} at about 160 cm⁻¹ can be well confirmed, while the E_g mode below 100 cm⁻¹ is ambiguous. The discrepancy of the low-frequency E_g modes in the two experiments^{14,16} is more than 10 cm⁻¹, and meanwhile both observed frequencies of the E_g modes are about 20–30 cm⁻¹ higher than the theoretical result. Furthermore, the two high-frequency Raman active modes (B_{1g} and E_g) have not been observed in all the experiments^{14,16,37,38} in spite of the high intensity of the B_{1g} mode in our calculations. The possible reason is due to the phonon damping caused by the large carrier concentration in Bi₂O₂Se, as indicated in Pereira's work.³⁷

The Raman spectrum of Bi₂O₂Te was also measured in Cheng's work,³⁸ which is listed in Table 5. The two observed Raman modes (A_{1g} and B_{1g}) are well consistent with our calculations. However, the two E_g modes are not observed in

Table 5 Comparison between calculated and experimental Raman frequencies of Bi₂O₂Te

	Raman frequency (cm ⁻¹)
This work	69.1 (E _g), 147.48 (A _{1g}), 336.0 (B _{1g}), 396.1 (E _g)
Experiment ³⁸	147 (A _{1g}), 340 (B _{1g})

their work. It is interesting to point out that the missing B_{1g} mode in Bi₂O₂Se was observed in Bi₂O₂Te, although in a relatively low intensity compared to that of the A_{1g} mode. Therefore, the Raman spectra of Bi₂O₂Se and Bi₂O₂Te need further investigations. For example, one could try to measure the Raman spectrum of Bi₂O₂Se with a lower carrier concentration by doping or at low temperatures in a proper Raman polarized configuration.

3.3 Pnmm orthorhombic Bi₂O₂S

Although Bi₂O₂S has a very similar crystal structure to the one of Bi₂O₂Se shown in Fig. 1(a) and (b), they have a different symmetry. In fact, Bi₂O₂S has an orthorhombic crystal structure with a space group of Pnmm (point group D_{2h}). There are ten atoms in the unit cell of Bi₂O₂S resulting in thirty phonon modes. Its irreducible representations at the Γ point are presented as follows:

$$\Gamma_{\text{acoustic}} = B_{1u} + B_{2u} + B_{3u}$$

$$\Gamma_{\text{optic}} = 3A_u + 2B_{1u} + 5B_{2u} + 5B_{3u} + 4A_g + 4B_{1g} + 2B_{2g} + 2B_{3g}$$

The calculated zone-centered optical phonon frequencies of Bi₂O₂S and their symmetries are listed in Table 6. It is found that all of the modes are non-degenerate. According to the character table of the D_{2h} point group, the B_{1u}, B_{2u}, and B_{3u} modes are IR active, while the A_g, B_{1g}, B_{2g} and B_{3g} modes are Raman active. The A_u modes are neither IR nor Raman active. From our calculation, Bi₂O₂S should have twelve Raman and twelve IR active modes, as shown in Table 6.

The vibrational eigenvectors of all the zone-centered optical modes and the polarized configurations of the Raman active modes are shown in Fig. S1 and Tables S1 and S2 in the ESI.†

IR and Raman intensities of Bi₂O₂S are also calculated directly by first principles calculations, which are shown in Fig. 4. It is found that the IR modes near 60, 290 and 400 cm⁻¹ have the highest intensities. In the Raman spectrum, the three

Table 6 Mulliken symbols and frequencies of zone-centered optical phonon modes of Bi₂O₂S. Raman or IR activity of each mode is also indicated by "Raman" and "IR". The A_u mode is neither Raman nor IR active. The unit of the phonon frequency is cm⁻¹

Symmetry	Bi ₂ O ₂ S	Activity	Symmetry	Bi ₂ O ₂ S	Activity
B _{2g}	9.5	Raman	B _{3u}	218.8	IR
A _g	13.9	Raman	A _g	285.2	Raman
A _u	53.7		B _{3u}	286.3	IR
B _{2u}	54.9	IR	B _{2g}	287.7	Raman
B _{3u}	60.7	IR	B _{1u}	288.5	IR
B _{1u}	64.9	IR	B _{3u}	364.4	IR
B _{3g}	65.2	Raman	A _g	367.8	Raman
B _{1g}	67.9	Raman	B _{2u}	404.2	IR
B _{2u}	75.7	IR	A _u	448.9	
B _{1g}	83.0	Raman	B _{1g}	450.6	Raman
A _u	113.1		B _{3g}	452.4	Raman
B _{2u}	113.4	IR	B _{2u}	457.5	IR
B _{3u}	144.7	IR	B _{1g}	519.1	Raman
A _g	170.6	Raman			



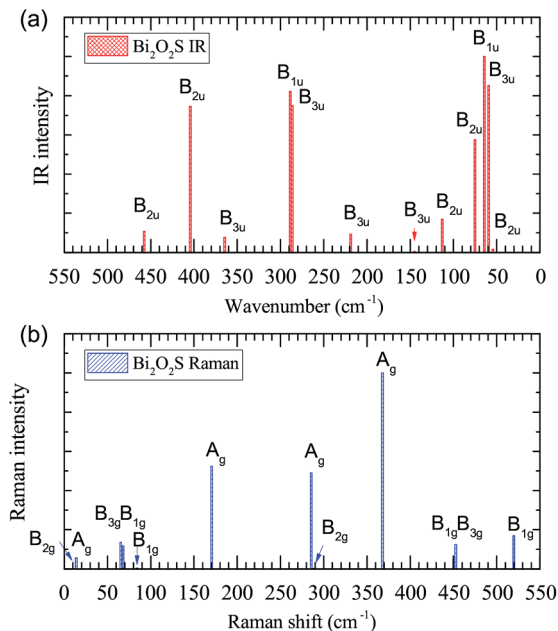


Fig. 4 Calculated IR and Raman intensities (arbitrary unit) of orthorhombic $\text{Bi}_2\text{O}_2\text{S}$.

A_g modes near 170, 285, and 370 cm^{-1} have the highest intensities.

It is noted that $\text{Bi}_2\text{O}_2\text{S}$ has been synthesized in experiments,^{24–26} however no Raman spectrum was measured yet. Recently, Cheng *et al.* have also calculated the Raman spectrum of $\text{Bi}_2\text{O}_2\text{S}$ by the density functional perturbation theory in the local density approximation and norm-conserving pseudopotentials implemented in Quantum Espresso (QE) software.³⁸ We listed their data in Table 7 as well as ours for comparison. From the frequency perspective, we can see that the two calculations are in general consistent with each other. For example, in both works, there are five Raman modes below 100 cm^{-1} , one mode between 100–200 cm^{-1} , two modes between 200–300 cm^{-1} , and *etc.* Although the largest difference in a B_{1g} mode reaches 43 cm^{-1} (about 10%), we still think it is acceptable since the two works use totally different methods in their calculations.

However, we noted that the Mulliken symbols in the two works are quite different. In particular, the four A_g modes in Cheng's work are all below 200 cm^{-1} , while we have two A_g modes below 200 cm^{-1} and two other ones above 200 cm^{-1} . The highest A_g mode in our work is more than 210 cm^{-1} higher than theirs. This cannot be explained by the inaccuracy of the phonon frequency induced by the different parameters. It is possibly due to the different classification of the Mulliken

symbols. In the D_{2h} point group, the assignment of B_{1g} , B_{2g} , and B_{3g} depends on the three mutually perpendicular 2-fold axes along the z , y , and x directions.⁵⁶ We have tested that QE software will give different Mulliken symbols (B_{1g} , B_{2g} , and B_{3g}) depending on the orientations of the orthorhombic unit cell of $\text{Bi}_2\text{O}_2\text{S}$. However, the assignment of the A_g mode should be unambiguous, which is independent of the directions of the unit cell. Therefore, we think the discrepancy of the A_g Raman modes in our work and Cheng's work needs further investigations.

3.4 $P4/nmm$ tetragonal Bi_2OS_2 , Bi_2OSe_2 , and Bi_2OTe_2

In experiment, Bi_2OS_2 has a space group of $P4/mmm$ (point group D_{4h}).^{28,55} However, to the best of our knowledge, Bi_2OSe_2 and Bi_2OTe_2 have not been synthesized in experiment. First principles calculations indicate that they share the same crystal structure as Bi_2OS_2 .³⁰ There are ten atoms in the unit cell of Bi_2OX_2 ($X = \text{S}, \text{Se}, \text{and Te}$) as shown in Fig. 1(c), resulting in thirty phonon modes. The irreducible representations of Bi_2OX_2 at the Γ point are:

$$\Gamma_{\text{acoustic}} = E_u + A_{2u}$$

$$\Gamma_{\text{optic}} = 4E_u + 4A_{2u} + 5E_g + 4A_{1g} + B_{1g}$$

The zone-centered optical phonon frequencies and their symmetries of Bi_2OX_2 are listed in Table 8. The vibrational eigenvectors of Bi_2OS_2 are shown in Fig. S2 in the ESI.† The polarized configurations of the Raman spectra of Bi_2OX_2 should be the same as those of $\text{Bi}_2\text{O}_2\text{Se}$ (Table 3) since they all belong to the D_{4h} point group.

According to the character table for the D_{4h} point group, the E_u and A_{2u} modes are IR active, while the E_g , A_{1g} , and B_{1g} modes are Raman active. Therefore, there are ten Raman active (five double degenerated E_g modes, five non-degenerated A_{1g} and B_{1g} modes) and eight IR active modes (four double degenerated E_u modes and four non-degenerated A_{2u} ones) in Bi_2OX_2 .

The IR and Raman intensities of Bi_2OX_2 are also calculated directly by first principles calculations, which are shown in Fig. 5. It is found that in the IR spectrum of Bi_2OS_2 , there are six modes (E_u modes around 98, 127, 262 cm^{-1} and A_{2u} modes around 129, 286, 466 cm^{-1}) which have relatively high intensities. For the Bi_2OSe_2 and Bi_2OTe_2 , only four modes have high intensities. For the Raman spectra of Bi_2OS_2 and Bi_2OSe_2 , there are two promising A_{1g} peaks around 132 and 346 cm^{-1} for Bi_2OS_2 , and 89 and 218 cm^{-1} for Bi_2OSe_2 . For Bi_2OTe_2 , the A_{1g} Raman mode around 163 cm^{-1} has the highest intensity.

Table 7 Comparison between the theoretical Raman frequencies of $\text{Bi}_2\text{O}_2\text{S}$. For each row, the Raman modes are arranged according to their frequencies. The unit of the phonon frequency is cm^{-1}

This work	B_{2g}	A_g	B_{3g}	B_{1g}	B_{1g}	A_g	A_g	B_{2g}	A_g	B_{1g}	B_{3g}	B_{1g}
	9.5	13.9	65.2	67.9	83.0	170.6	285.2	287.7	367.8	450.6	452.4	519.1
Cheng ³⁸	B_{2g}	A_g	B_{2g}	A_g	A_g	A_g	B_{1g}	B_{3g}	B_{1g}	B_{1g}	B_{3g}	B_{1g}
	20.52	29.23	64.34	68.23	82.86	154.20	263.85	273.27	386.85	407.76	417.30	520.28



- 11 C. Wang, G. Q. Ding, X. M. Wu, S. S. Wei and G. Y. Gao, *New J. Phys.*, 2018, **20**, 123014.
- 12 C. Drasar, P. Ruleova, L. Benes and P. Lostak, *J. Electron. Mater.*, 2012, **41**, 2317.
- 13 J. X. Wu, H. T. Yuan, M. M. Meng, C. Chen, Y. Sun, Z. Y. Chen, W. H. Dang, C. W. Tan, Y. J. Liu, J. B. Yin, Y. B. Zhou, S. Y. Huang, H. Q. Xu, Y. Cui, H. Y. Hwang, Z. F. Liu, Y. L. Chen, B. H. Yan and H. L. Peng, *Nat. Nanotechnol.*, 2017, **12**, 530.
- 14 J. X. Wu, C. W. Tan, Z. J. Tan, Y. J. Liu, J. B. Yin, W. H. Dang, M. Z. Wang and H. L. Peng, *Nano Lett.*, 2017, **17**, 3021.
- 15 C. Chen, M. X. Wang, J. X. Wu, H. X. Fu, H. F. Yang, Z. Tian, T. Tu, H. Peng, Y. Sun, X. Xu, J. Jiang, N. B. M. Schröter, Y. W. Li, D. Pei, S. Liu, S. A. Ekahana, H. T. Yuan, J. M. Xue, G. Li, J. F. Jia, Z. K. Liu, B. H. Yan, H. L. Peng and Y. L. Chen, *Sci. Adv.*, 2018, **4**, eaat8355.
- 16 T. Tong, M. Zhang, Y. Chen, Y. Li, L. Chen, J. Zhang, F. Song, X. Wang, W. Zou, Y. Xu and R. Zhang, *Appl. Phys. Lett.*, 2018, **113**, 072106.
- 17 Y. Y. Lv, L. Xu, S. T. Dong, Y. C. Luo, Y. Y. Zhang, Y. B. Chen, S. H. Yao, J. Zhou, Y. S. Cui, S. T. Zhang, M. H. Lu and Y. F. Chen, *Phys. Rev. B*, 2019, **99**, 195143.
- 18 H. X. Fu, J. X. Wu, H. L. Peng and B. H. Yan, *Phys. Rev. B*, 2018, **97**, 241203.
- 19 Y. Y. Lv, X. Li, J. L. Zhang, B. Pang, S. S. Chen, L. Cao, B. B. Zhang, D. J. Lin, Y. B. Chen, S. H. Yao, J. Zhou, S. T. Zhang, M. H. Lu, M. L. Tian and Y. F. Chen, *Phys. Rev. B*, 2018, **97**, 245151.
- 20 J. Li, Z. X. Wang, Y. Wen, J. W. Chu, L. Yin, R. Q. Cheng, L. Lei, P. He, C. Jiang, L. P. Feng and J. He, *Adv. Funct. Mater.*, 2018, **28**, 1706437.
- 21 J. X. Wu, Y. J. Liu, Z. J. Tan, C. W. Tan, J. B. Yin, T. R. Li, T. Tu and H. L. Peng, *Adv. Mater.*, 2017, **29**, 1704060.
- 22 J. Yin, Z. Tan, H. Hong, J. Wu, H. Yuan, Y. Liu, C. Chen, C. Tan, F. Yao, T. Li, Y. Chen, Z. Liu, K. Liu and H. Peng, *Nat. Commun.*, 2018, **9**, 3311.
- 23 S. D. N. Luu and P. Vaqueiro, *J. Solid State Chem.*, 2015, **226**, 219.
- 24 E. Koyama, I. Nakai and K. Nagashima, *Acta Crystallogr., Sect. B: Struct. Sci.*, 1984, **40**, 105.
- 25 A. L. Pacquette, H. Hagiwara, T. Ishihara and A. A. Gewirth, *J. Photochem. Photobiol., A*, 2014, **277**, 27.
- 26 Í. A. Kariper, *Spectrochim. Acta, Part A*, 2016, **163**, 102.
- 27 X. Zhang, Y. Liu, G. Zhang, Y. Wang, H. Zhang and F. Huang, *ACS Appl. Mater. Interfaces*, 2015, **7**, 4442.
- 28 A. Miura, Y. Mizuguchi, T. Takei, N. Kumada, E. Magome, C. Moriyoshi, Y. Kuroiwa and K. Tadanaga, *Solid State Commun.*, 2016, **227**, 19.
- 29 X. W. Zhang, B. Wang, X. H. Niu, Y. H. Li, Y. F. Chen and J. L. Wang, *Mater. Horiz.*, 2018, **5**, 1058.
- 30 X. Ma, D. Chang, C. Zhao, R. Li, X. Huang, Z. Zeng, X. Huang and Y. Jia, *J. Mater. Chem. C*, 2018, **6**, 13241.
- 31 S. Azam, S. A. Khan and S. Goumri-Said, *J. Electron. Mater.*, 2018, **47**, 2513.
- 32 S. K. Singh, A. Kumar, B. Gahtori, S. G. Sharma, S. Patnaik and V. P. S. Awana, *J. Am. Chem. Soc.*, 2012, **134**, 16504.
- 33 Y. Mizuguchi, H. Fujihisa, Y. Gotoh, K. Suzuki, H. Usui, K. Kuroki, S. Demura, Y. Takano, H. Izawa and O. Miura, *Phys. Rev. B: Condens. Matter Mater. Phys.*, 2012, **86**, 220510(R).
- 34 W. A. Phelan, D. C. Wallace, K. E. Arpino, J. R. Neilson, K. J. Livi, C. R. Seabourne, A. J. Scott and T. M. McQueen, *J. Am. Chem. Soc.*, 2013, **135**, 5372.
- 35 L. Li, D. Parker, P. Babkevich, L. Yang, H. M. Ronnow and A. S. Sefat, *Phys. Rev. B: Condens. Matter Mater. Phys.*, 2015, **91**, 104511.
- 36 J. F. Shao, Z. H. Liu, X. Yao, L. Pi, S. Tan, C. J. Zhang and Y. H. Zhang, *Phys. Status Solidi RRL*, 2014, **8**, 845.
- 37 A. L. J. Pereira, D. Santamaría-Pérez, J. Ruiz-Fuertes, F. J. Manjón, V. P. Cuenca-Gotor, R. Vilaplana, O. Gomis, C. Popescu, A. Muñoz, P. Rodríguez-Hernández, A. Segura, L. Gracia, A. Beltraán, P. Ruleova, C. Drasar and J. A. Sans, *J. Phys. Chem. C*, 2018, **122**, 8853.
- 38 T. Cheng, C. W. Tan, S. Q. Zhang, T. Tu, H. L. Peng and Z. R. Liu, *J. Phys. Chem. C*, 2018, **122**, 19970.
- 39 G. Kresse and J. Furthmüller, *Comput. Mater. Sci.*, 1996, **6**, 15.
- 40 G. Kresse and J. Furthmüller, *Phys. Rev. B: Condens. Matter Mater. Phys.*, 1996, **54**, 11169.
- 41 P. E. Blöchl, *Phys. Rev. B: Condens. Matter Mater. Phys.*, 1994, **50**, 17953.
- 42 G. Kresse and D. Joubert, *Phys. Rev. B: Condens. Matter Mater. Phys.*, 1999, **59**, 1758.
- 43 J. P. Perdew, K. Burke and M. Ernzerhof, *Phys. Rev. Lett.*, 1996, **77**, 3865.
- 44 S. Grimme, J. Antony, S. Ehrlich and H. Krieg, *J. Chem. Phys.*, 2010, **132**, 154104.
- 45 S. Grimme, S. Ehrlich and L. Goerigk, *J. Comput. Chem.*, 2011, **32**, 1456.
- 46 A. Togo and I. Tanaka, *Scr. Mater.*, 2015, **108**, 1.
- 47 K. Momma and F. Izumi, *J. Appl. Crystallogr.*, 2011, **44**, 1272.
- 48 P. Giannozzi and S. Baroni, *J. Chem. Phys.*, 1994, **100**, 8537.
- 49 J. Zhou and J. Dong, *J. Appl. Phys.*, 2010, **107**, 024306.
- 50 D. Karhánek, T. Bučko and J. Hafner, *J. Phys.: Condens. Matter*, 2010, **22**, 265006.
- 51 K. Esfarjani, Y. Hashi, J. Onoe, K. Takeuchi and Y. Kawazoe, *Phys. Rev. B: Condens. Matter Mater. Phys.*, 1998, **57**, 223.
- 52 A. Fonari and S. Stauffer, vasp_raman.py, <https://github.com/raman-sc/VASP/>.
- 53 J. M. Skelton, L. A. Burton, A. J. Jackson, F. Oba, S. C. Parker and A. Walsh, *Phys. Chem. Chem. Phys.*, 2017, **19**, 12452.
- 54 D. T. Larson and E. Kaxiras, *Phys. Rev. B*, 2018, **98**, 085406.
- 55 N. Takahashi, M. Nagao, A. Miura, S. Watauchi, K. Tadanaga, Y. Takano and I. Tanaka, *J. Ceram. Soc. Jpn.*, 2018, **126**, 591.
- 56 R. S. Mulliken, *J. Chem. Phys.*, 1955, **23**, 1997.

